Hindawi
International Journal of RF and Microwave Computer-Aided Engineering
Volume 2023, Article ID 2679182, 20 pages
https://doi.org/10.1155/2023/2679182

Research Article

A Compact Tri-Band Penta-Polarization Reconfigurable Planar Antenna for Interference Management in 5G Ultra-Dense Network Environment

Joydeep Pal and Bhaskar Gupta

Jadavpur University, Kolkata, 700032 West Bengal, India

Correspondence should be addressed to Joydeep Pal; joybtech@gmail.com

Received 5 November 2022; Revised 29 June 2023; Accepted 18 July 2023; Published 17 August 2023

Academic Editor: Ashish Bagwari

Interference and multipath are the most common issues in the wireless domain due to the coexistence of a large number of wireless nodes operating within the constraint spectrum. A compact planar antenna with five reconfigurable polarization states in three distinct operating bands is presented in this article. A square patch is enclosed by a square outer ring in the design, and these antennas are coupled-decoupled successively using switching diodes to excite three distinct operating bands. Coplanar microstrip lines are used to feed the orthogonal edges of the antenna. The diagonal corners of the inner and outer ring patches are truncated to realize dual circular polarization (CP) states with proper biasing. Switching diodes are placed at the etched corners to realize vertical (VP) and horizontal (HP) polarization. Both the orthogonal feed lines are activated simultaneously with identical phase and amplitude to realize 45° linear polarization. A low-profile, single-feed, compact prototype reconfigurable microstrip antenna (MSA) is finally designed, fabricated, and measured at 1.8 GHz, 2.4 GHz, and 5.8 GHz bands, respectively. Each operating band shows five distinct operating states. The simulation results for all fifteen states are found to be consistent with the measurement.

1. Introduction

The progress on the wireless front is happening very rapidly to cater to diverse multifacet applications such as IoT, automation, remote sensing, geopositioning with larger accuracy, healthcare, security, and space application [1]. Several wireless nodes in point-to-point or multipoint (P2P or P2MP) links are being deployed in close proximity to enhance network coverage and capacity in the present and impending heterogeneous network architecture [2]. These nodes are operating within the limited available spectrum, causing intersystem and cochannel interference issues resulting in randomly fluctuating received signal strength (RSS). The mentioned issues along with multipath in the wireless channel also cause a higher BER (bit error rate) and reduced SINR (signal to interference and noise ratio) [3]. Researchers have dealt with these very issues from a signal processing and communication perspective [4, 5]. The prime motivation of this work is to deal with these issues from an RF standpoint and to provide system designers with an additional degree of freedom. Thus, multifunctional antennas are incorporated into the transreceiver system design to normalize the mentioned issues on the wireless front to a great extent. In this article, a tri-band and penta-polarization agile mirostrip patch antenna (MSA) is proposed at the earliest in the open literature. The mentioned flow chart in Figure 1 depicts the working procedure of the proposed antenna to mitigate those issues. In a dense RF environment, the probability of signal interference and quality degradation is very high. In such scenarios, the polarization of a P2P/P2MP (point-to-point or point-to-multipoint) RF link operating at a specific band is altered to another polarization to achieve a larger received signal strength (RSS) than the threshold RSS value and a higher SINR with improved BER [6] of the operating RF link. The operating band is changed if a stable state is not achieved by changing all available polarization states at that specific band. Similarly, in the changed frequency band too, all available polarization states are altered to attain

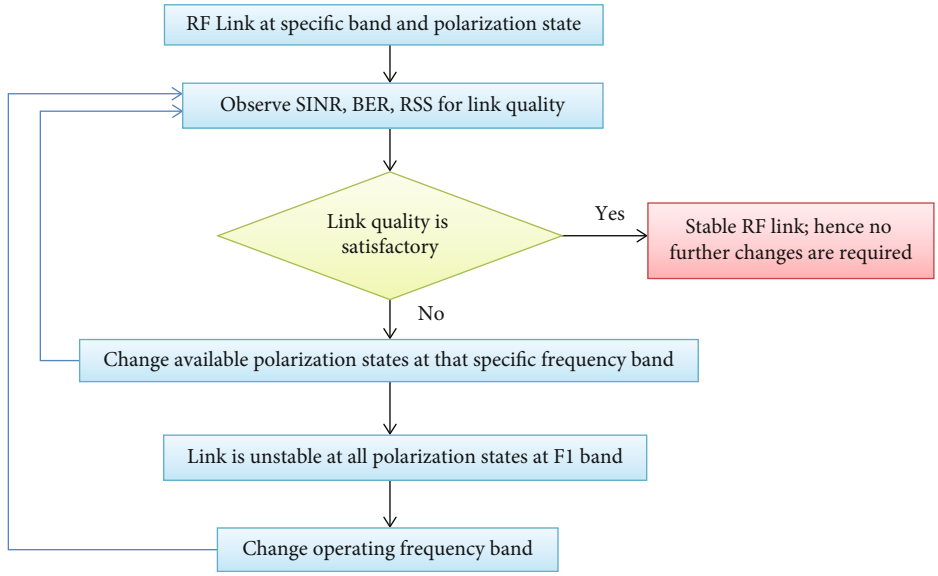

Figure 1: Flowchart of the working process of the proposed tri-band penta-polarization agile MSA to mitigate interference and fading effect in an ultradense network environment.

optimum signal quality in terms of low BER and high SINR. Thus, the proposed antenna provides large flexibility with fifteen reconfigurable states for the system designers.

In the open literature, authors have proposed a maximum up-to-quad polarization state in single or multiple operating bands. It is noted in the literature that authors have used complex and advanced techniques to attain multifunction antennas. These techniques are mostly based on high impedance surfaces (HIS) or metasurface, liquid metal, surface plasmon polariton (SPP), artificial magnetic conductor [7, 8], orbital angular momentum (OAM), DRAs (dielectric resonator antenna), and magneto-electric dipole. An AMC- (artificial magnetic conductor-) based dual feed monopole planar antenna is proposed in [7] for dual band and polarization agility. A tri-band dual-polarized microstrip antenna (MSA) array is proposed in [9]. Also, a dual-band, quad-polarization reconfigurable MSA is shown in [10]. In a recently proposed antenna [11], multiple polarization states are attained in different operating bands. In our previous article [12], we proposed a microstrip antenna (MSA) that operates in two distinct bands, and both bands are further reconfigured at penta-polarization states. Previously, only one article on a metasurface-inspired microstrip slot antenna [13] with five reconfigurable polarization states was discussed in the literature. The important observation is that all the recently proposed antennas with advanced techniques suffer from several unavoidable complications. Firstly, most of the antennas are having multilayer, high-profile bulky structures which impose significant difficulties in antenna fabrication. Secondly, most of the antennas are having multiple feed ports which cause problems in system integration or interfacing the antenna with other devices in the transreceiver system. Thirdly, the electromechanical mechanism to control the liquid metal in reconfigurable liquid antennas is extremely cumbersome. Finally, the asymmetric structure with a complex feed network and large footprint area imposes difficulties for practical realization. In contrast, the projected design shows the mentioned advantages and novelty.

(1) A compact, simple, low-profile MSA ($0.9\lambda_0 \times 0.9\lambda_0 \times 0.01\lambda_0$) with fifteen different reconfigurable states with five reconfigurable polarization states at three operating bands is projected for the very first time in the open literature

(2) This design can be scaled to different frequencies; hence, scalability makes the proposed design appropriate for a very large variety of applications in the upcoming heterogeneous network

(3) The antenna provides great flexibilities to the system designers with fifteen distinct reconfigurable states to attain optimum signal quality in electromagnetically dense environments. In the current heterogeneous network domain, the proposed antenna is suitable for diverse applications due to its simple design, ease of fabrication, compactness, and scalability

2. Antenna Design Concept

2.1. Concept behind Frequency Agility. A square microstrip antenna (MSA) (highlighted section) operates on the higher frequency band ($f1$ at 5.8 GHz), as depicted in Figure 2(a). An outer square ring is interfaced with the inner patch using switching diodes, forms a larger patch as depicted in Figure 2(b), and operates at a lower frequency $f2$ (2.45 GHz). The lowest operating band $f3$ (1.8 GHz) is accomplished by exciting the outer square ring separately, as highlighted in Figure 2(c). Two rectangular slots are cut in the adjacent edges of the outer ring to allow feed lines to connect with the inner patch, as shown in Figure 2. To excite the outer and inner patches with proper bias, reconfigurable planar feed lines are

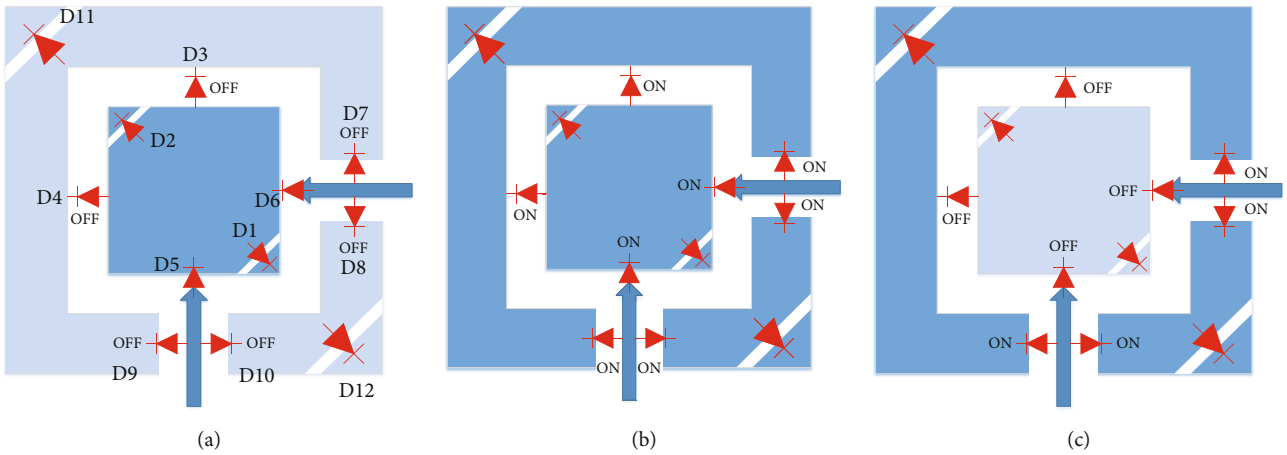

FIGURE 2: Prototype antenna structures for three reconfigurable bands with suitable diode biasing conditions, (a) $f1$, (b) $f2$, and (c) $f3$.

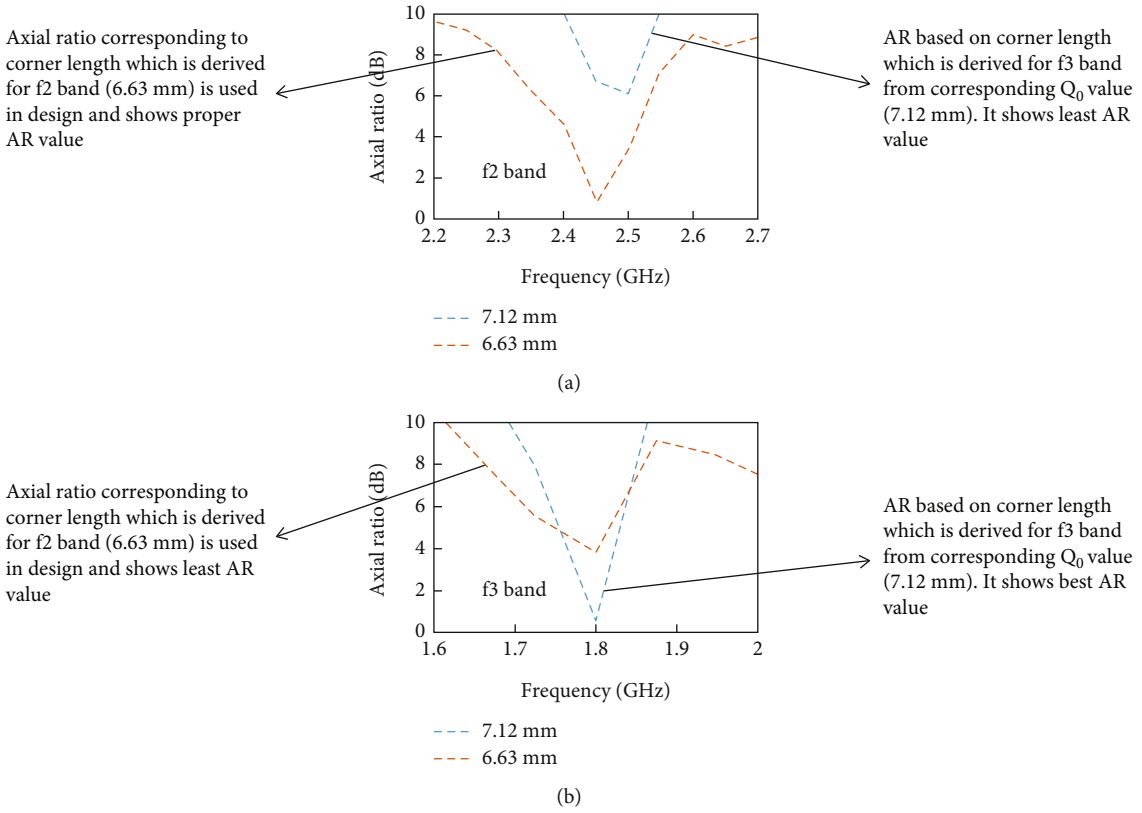

FIGURE 3: LHCP axial ratios based on corner lengths which are derived from the Q0 values of the $f2$ and $f3$ bands (a) AR at $f2$ band corresponding to 6.63 mm and 7.12 mm corner lengths and (b) AR at $f3$ band corresponding to 6.63 mm and 7.12 mm corner lengths.

connected to the orthogonal patch edges. As shown in Figure 3(f), $f1$ and $f2$ are obtained from the edge lengths of the inner and outer square patches, given by (1) and (2), respectively. The lowest frequency band $f3$, due to the larger current path on the outer ring patch surface, is derived by (3).

$$f1 = \frac{c}{2b\sqrt{\varepsilon_{\text{eff}}}}, \tag{1}$$

$$f2 = \frac{c}{2a\sqrt{\varepsilon_{\text{eff}}}}, \tag{2}$$

$$f3 = \frac{c}{2(a+b)\sqrt{\varepsilon_{\text{eff}}}}, \tag{3}$$

where a and b are the edge lengths of inner and outer patch and ε_{eff} represents the effective dielectric constant of the substrate.

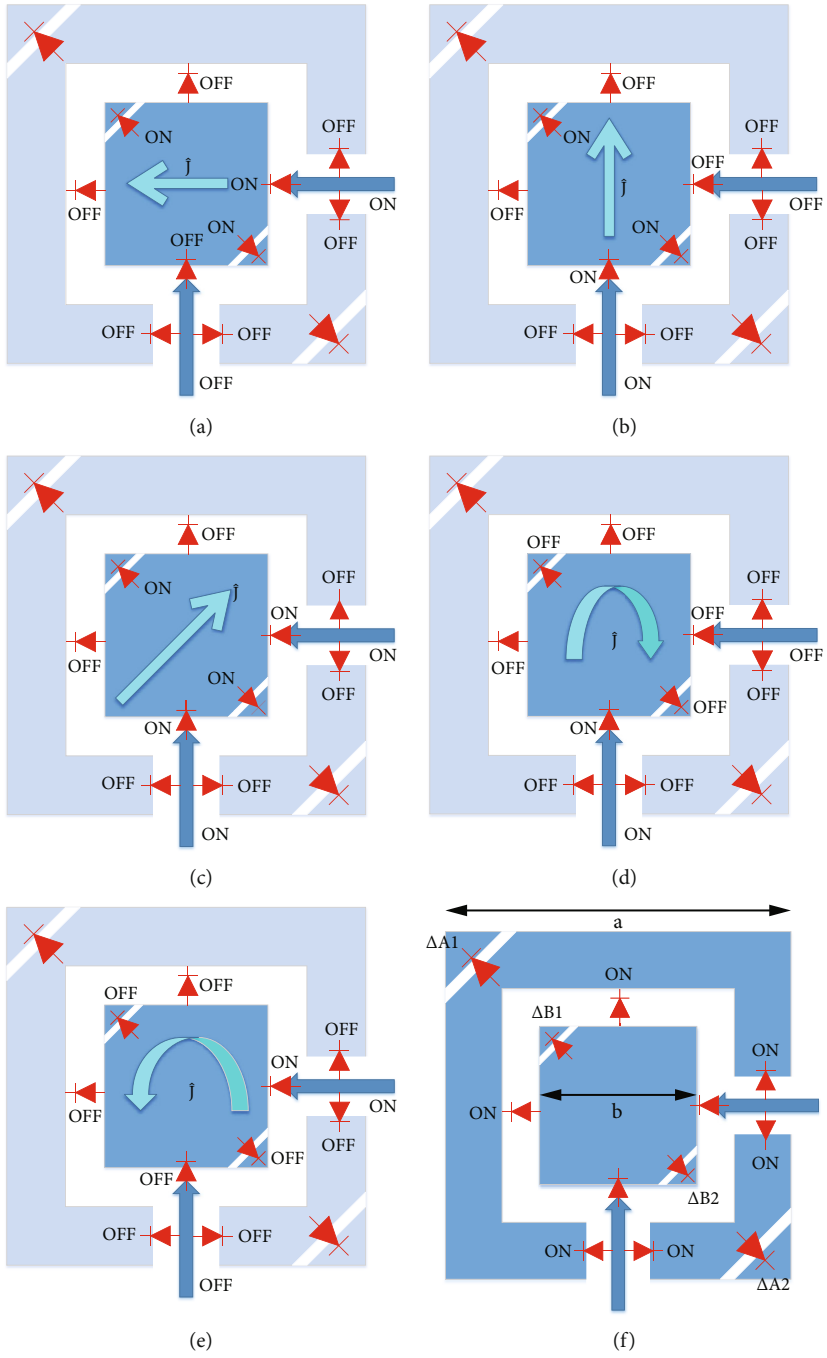

FIGURE 4: Illustration of the orientation of surface currents on the prototype antenna at f1 band for penta-polarization states (a) HP, (b) VP, (c) 45° slant (d) LHCP, (e) RHCP, and (f) prototype antenna structure using suitable biasing network.

Switching diodes are used to excite the vertical and horizontal feed lines as per the requirement of five distinct polarization states, as shown in Figure 4. The vertical line is excited to realize VP (vertical polarization) (Figure 4(b)) and LHCP (left hand circular polarization) (Figure 4(d)) states, while horizontal feed is activated to generate HP (horizontal polarization) (Figure 4(a)) and RHCP (right hand circular polarization) (Figure 4(e)) states. Subsequently, the feed lines are excited together to generate a 45° slant linear polarization (Figure 4(c)) state.

2.2. Polarization Reconfiguribility. The diagonal corner truncation of a square MSA to generate the orthogonal modes, i.e., TM_{10} and TM_{01}, respectively, for CP (circular polarization) generation is well studied in the literature [14].The area of the truncated corners is related with the quality factor of the antenna using (4) to initiate the CP states.

$$\frac{\text{Total Area of the Truncated corner } (2 * \Delta A)}{\text{Total Area of the square patch } (A)} = \frac{1}{2 * \text{Quality Factor}(Q0)}. \tag{4}$$

Table 1: Diode biasing for tri-band penta-polarization states.

Freq.	Pol. states	D1 & D2	D3& D4	D5	D6	D7& D8	D9 &D15	D10 & D11	D12 & D13	D14
	VP	Off	Off	On	Off	Off	Off	Off	Off	On
	HP	Off	Off	Off	On	Off	On	Off	Off	Off
$f1$	45°	Off	Off	On	On	Off	On	Off	Off	On
	RHCP	Off	Off	Off	On	Off	On	Off	Off	On
	LHCP	Off	Off	On	Off	Off	Off	Off	Off	On
	VP	On	On	On	Off	On	Off	On	On	On
	HP	On	On	Off	On	On	On	On	On	Off
$f2$	45°	On	On	On	On	On	On	On	On	On
	RHCP	Off	Off	Off	On	On	On	On	Off	On
	LHCP	Off	On	On	Off	On	Off	On	Off	On
	VP	On	Off	Off	Off	On	Off	On	On	On
	HP	On	Off	Off	Off	On	On	On	On	Off
$f3$	45°	On	Off	Off	Off	On	On	On	On	On
	RHCP	On	Off	Off	Off	On	On	On	Off	Off
	LHCP	On	Off	Off	Off	On	Off	On	Off	On

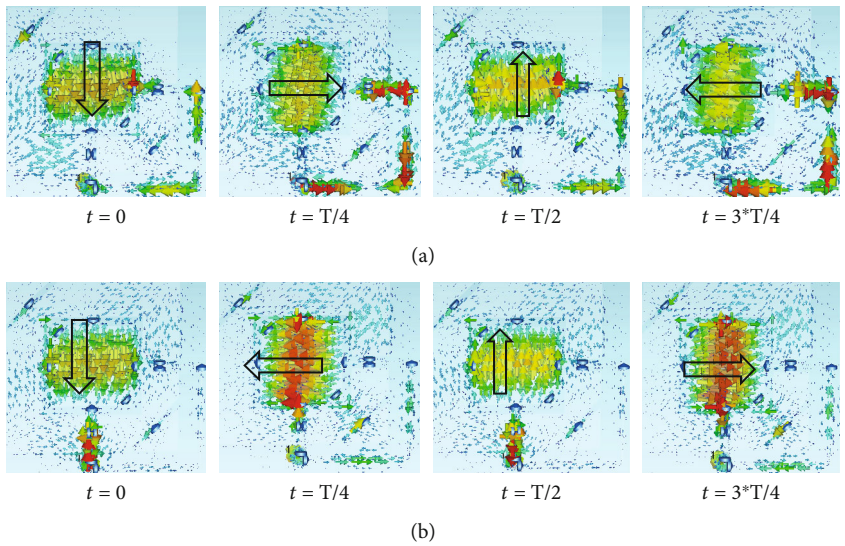

Figure 5: Current distribution on the MSA surface for successive T/4 time at $f1$ band for (a) RHCP and (b) LHCP.

The inner and outer patch corners are truncated as illustrated in the diagram to attain CP states at all operating bands. The frequencies of the orthogonal modes of the near square patch antenna is illustrated in (5) and (6), respectively.

$$f_x = f_1\left(1 - \frac{2\Delta B}{B}\right), \tag{5}$$

$$f_y = f_1, \tag{6}$$

$$Q_0 = \frac{f_0}{\Delta f}, \tag{7}$$

where $\Delta B(=\Delta B1 + \Delta B2)$ is the overall area of both the diagonal corners, as shown in Figure 3(f). Also, $B = b^2$ is the total area, as shown in Figure 4(f). Subsequently, the orthogonal frequencies for combined square patch (for $f2$ band) and the outer ring ($f3$ band) as highlighted in Figure 2 are devised as follows:

$$f_x^2 = f_3\left(1 - \frac{2\Delta A}{A1}\right) < f_x^1 = f_2\left(1 - \frac{2\Delta A}{A}\right) < f_x, f_y^2 = f_3 < f_y^1 = f_2 < f_y, \tag{8}$$

where $\Delta A = \Delta A1 + \Delta A2$ is the area of the total truncated sections of the outer ring and $A = a^2$ (total area of the combined patch) while considering combined inner-outer patch for $f2$ operation, as illustrated in Figure 4(f). Subsequently, $A1 = b^2 - w^2$, where w is the inner edge length of the outer ring patch for $f3$ band operation. The truncated corners of

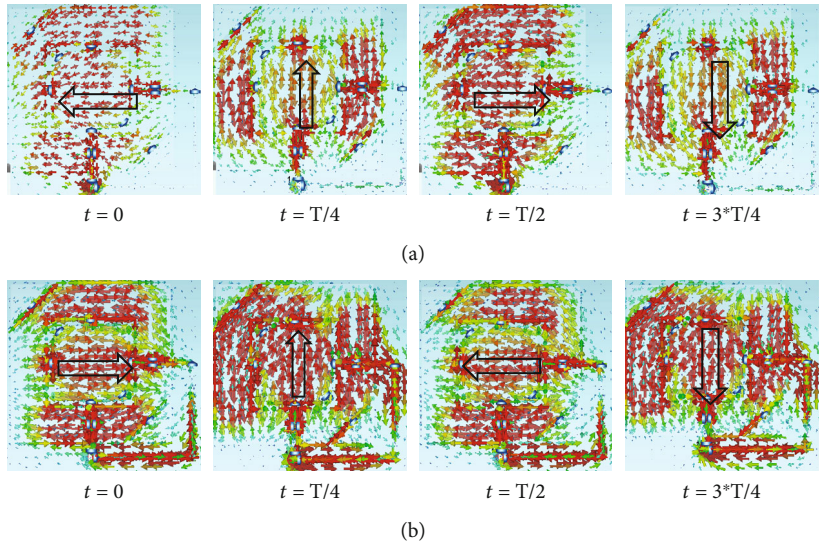

FIGURE 6: Current distribution on the MSA surface for successive T/4 time at $f2$ band for (a) LHCP and (b) RHCP.

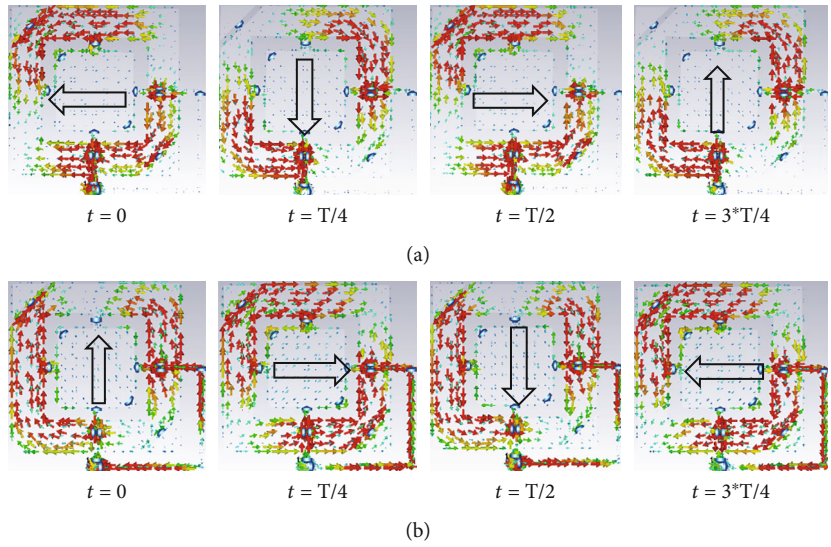

FIGURE 7: Current distribution on the MSA surface for successive T/4 time at $f3$ band for (a) RHCP and (b) LHCP states.

the outer square ring patch are shared by band 2 and band 3. The values of Q_0 for five distinct polarization states at each band are derived from the simulated Z_{real} using (7). These derived Q_0 values are used to find the length of the truncated corner (ΔA) of the outer ring for band 2 and band 3 using (4) and are found to be 6.63 mm and 7.12 mm, respectively. The length of the truncated corners is slightly different as the bands are slightly different ($f2 = 2.45$ GHz and $f3 = 1.8$ GHz). If we design the antenna with an outer ring patch corner length of 6.63 mm, which is derived for $f2$ band, then a proper 3 dB AR value is observed for LHCP or RHCP states at $f2$ band but AR deteriorates in case of $f3$ band, as depicted in Figure 3(a). Similarly, considering corner length 7.12 mm (which is derived for $f3$ band) for the design exhibits a proper 3 dB AR of both the CP states at $f3$ frequency band, while the AR at $f2$ band for both the CP states deteriorates, as depicted in Figure 3(b). As both polarization states depict similar results, hence, only the LHCP state is shown in the plots for necessary illustration. It is observed that AR for both CP states in $f2$ and $f3$ band is primarily depend on the lengths of the inner (w) and outer (a) sides of the outer ring patch along with corner length (y) and corner slot width (x).

Complete parametric optimization of these above parameters is performed to achieve optimum 3 dB AR in all CP states in both frequency bands. It is noted that at the truncated length of 6.8 mm along with the other optimized parameters, the AR for all CP states at both bands depict suitable results, which are illustrated in Section 4. Figure 4 illustrates the generation of five distinct polarization states at $f1$ band by selectively choosing the vertical and

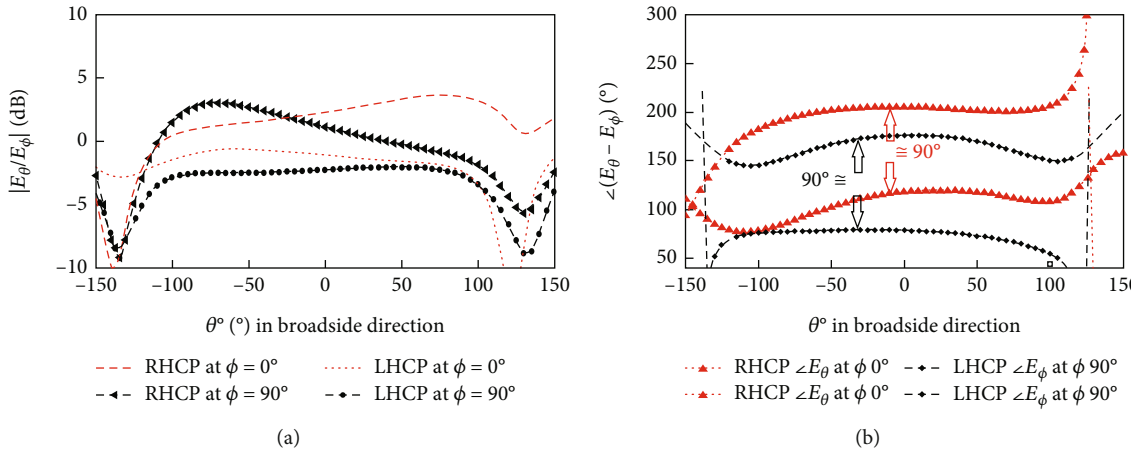

FIGURE 8: (a) Simulated amplitude ratios of $|E_\theta/E_\varphi|$ component and (b) simulated phase of $\angle(E_\theta - E_\varphi)$ for dual CPs at $\varphi = 0^\circ$ and 90° plane at $f2$ operating band.

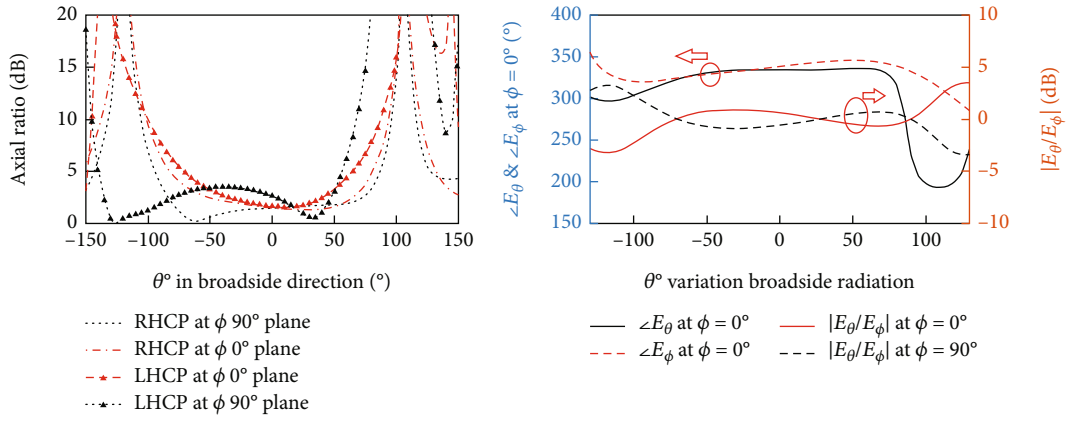

FIGURE 9: (a) Simulated axial ratios of the components at the far field at $\varphi = 0^\circ$ and 90° plane at $f2$ operating band and (b) simulated amplitude of E_θ and E_φ component ratios and phase of E_θ and E_φ components for 45° slant polarization at $\varphi = 0^\circ$ and 90° plane.

horizontal feed lines using proper switching diodes and biasing. Subsequently, 45° linear polarization is attained by exciting both feed lines together with equal phases and amplitudes, as shown in Figure 4(c). Diode biasing states for penta-polarization reconfigurability at three different bands are listed in Table 1.

2.2.1. Polarization Agility at $f1$ Band. Penta-polarization agility at $f1$ band is achieved using the diode biasing conditions, as illustrated in Table 1. The surface current of the inner patch for RHCP (Figure 5(a)) and LHCP (Figure 5(b)) states is shown in Figure 5 for T/4 successive time periods. This portrays the shortest $\lambda/2$ current path, which subsequently represents the upper frequency band ($f1 = 5.8$ GHz).

2.2.2. Polarization Agility at $f2$ Band. Five reconfigurable polarization states at $f2$ band are achieved using the diode biasing conditions, as illustrated in Table 1. The surface current of the combine patch for RHCP (Figure 6(b)) and LHCP (Figure 6(a)) states is shown in Figure 6 for successive T/4 time periods at $f2$ band (2.45 GHz).

2.2.3. $f3$ Band Polarization Agility. Five distinct polarization agilities at $f3$ band are achieved using the diode biasing conditions, as illustrated in Table 1. The surface current of the combine patch for RHCP (Figure 7(a)) and LHCP (Figure 7(b)) states is shown in Figure 7 for successive T/4 time periods at $f3$ band (1.8 GHz).

2.2.4. Analysis on the Generation of CP and 45° Linear Polarization. For detailed observation, the phase and magnitudes of the radiated electric components are analyzed in the broadside direction. Figure 8(a) illustrates the ratios of the $|E_\theta/E_\varphi|$ in dB in both the principal planes $\varphi = 0^\circ$ and 90°, respectively, at RHCP and LHCP states at $f2$ frequency band. The plot depicts that the ratios lied at ±1.5 dB,

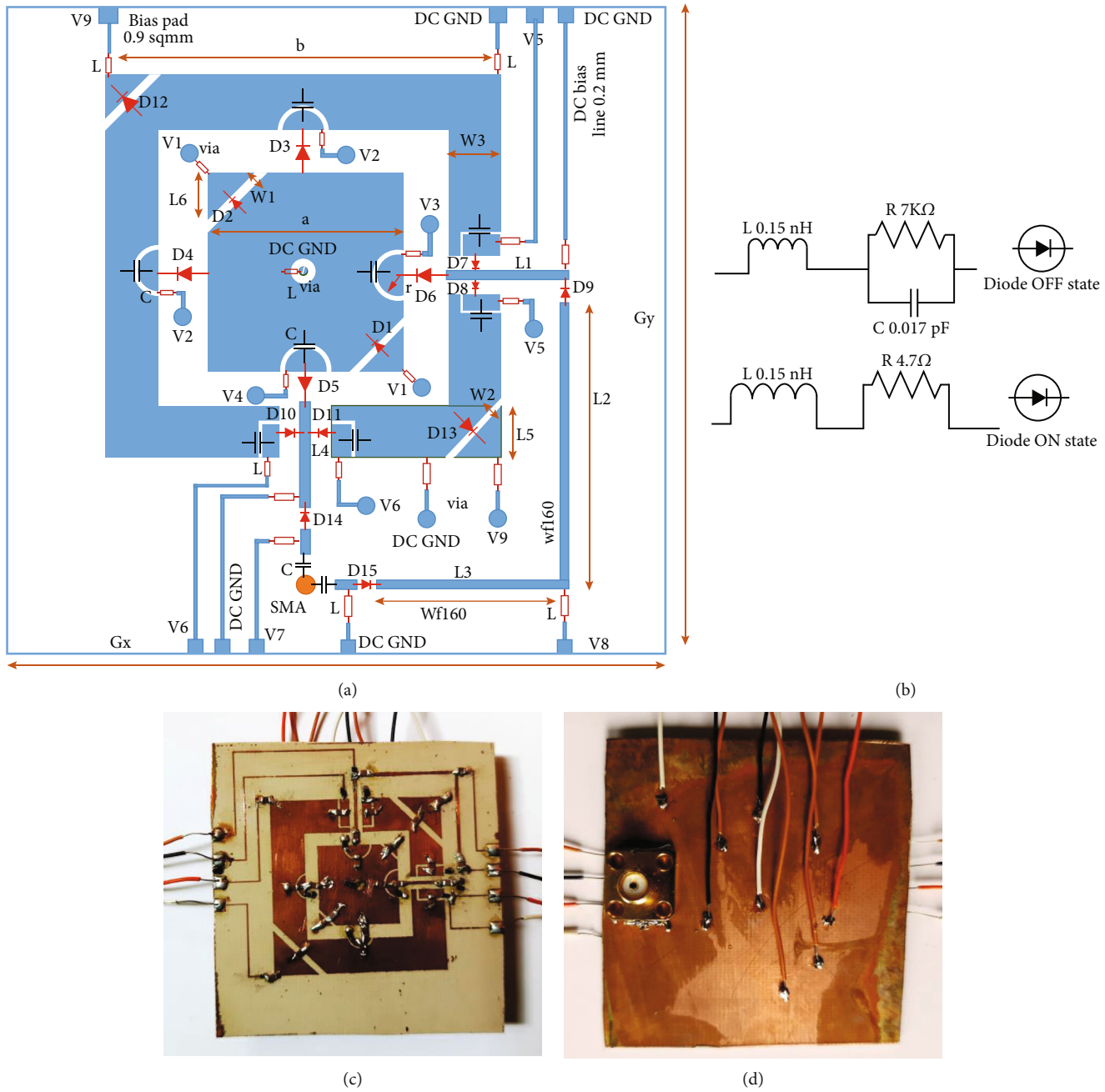

FIGURE 10: (a) Antenna diagram with complete feed network, switching diodes, bias network, and fabricated prototype antenna. (b) Equivalent diode model. (c) Top view. (d) Bottom view. Gx = Gy = 50, $a = 12.5$, $b = 27.2$, $L1 = 10.55$, $L2 = 15.73$, $L3 = 16.17$, $L4 = 8.2$, $L5 = 6.8$, $L6 = 1.3$, $W1 = 1$, $W2 = 0.32$, $W3 = 5.8$, $r = 3$, and $wf160 = 0.2$ (dimensions in mm).

exhibiting nearly equal magnitude along the half-power beam width (HPBW ± 53°) of the pattern.

Contrarily, the relative phase differences between the orthogonal components, i.e., $\angle(E_\theta - E_\varphi)$ in both the principal plane are nearly ±90° in the broadside direction and within the HPBW, as shown in Figure 8(b). Hence, the phase and magnitude of E_θ and E_φ are found appropriate for both LHCP and RHCP generation. Also, the axial ratio along the broadside direction within HPBW is found within 3 dB value in both the principal planes, as illustrated in Figure 9(a).

The relative phase and ratio of the orthogonal components E_θ and E_φ are also observed for 45° slat polarization state. The $|E_\theta/E_\varphi|$ in dB is found to remain within ±1 dB, while the phase difference $\angle(E_\theta - E_\varphi)$ at $\varphi = 0°$ and 90° planes is nearly zero ($\angle E_\theta = \angle E_\varphi$) along the HPBW at broadside direction, as illustrated in Figure 9(b). Similar observations are noted for $f1$ and $f3$ bands also, hence not shown for brevity.

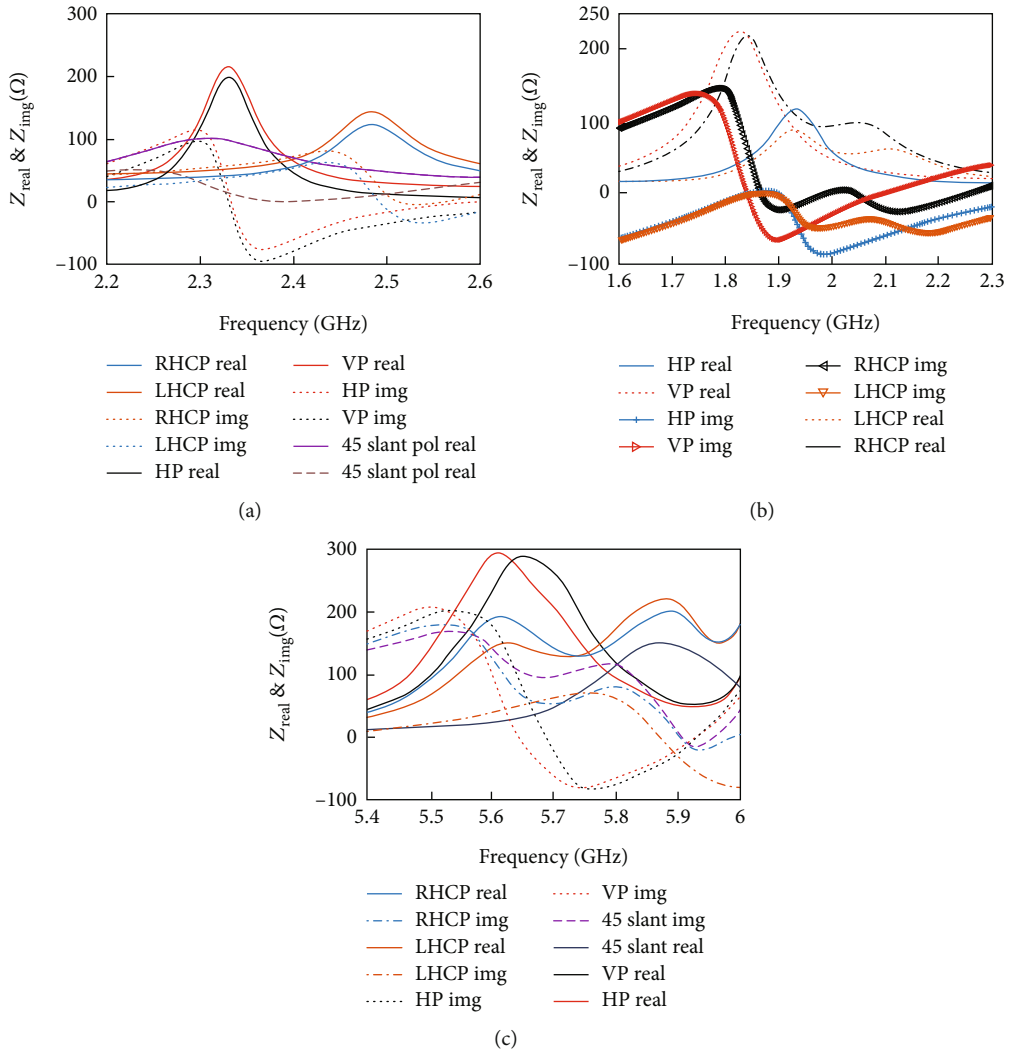

FIGURE 11: Real and imaginary part of the edge impedances of the prototype antenna for multiple polarization states at (a) $f1$, (b) $f2$, and (c) $f3$ band.

3. Prototype Antenna Design

To validate the proposed theory, a MSA that operates at 1.8 GHz ($f3$), 2.4 GHz ($f2$), and 5.8 GHz ($f1$) bands is designed and fabricated. These bands can further be reconfigured to generate penta-polarization states using the proper biasing networks presented in the subsequent sections. Roger RO404 substrate having dielectric constant $\varepsilon_r = 3.51$, loss tangent tan $\delta = 0.017$, and height $h = 30$ mil is used to fabricate the antenna. The complete layout of the simulated antenna is shown in Figure 10(a). A finite different time domain (FDTD) computational technique-based three-dimensional (3D) commercial electromagnetic simulator, computer simulation technologies (CST) of version 2019 (by Dassault Systems), is used for the entire simulation.

3.1. Antenna Feed Network Design and Optimization. The impedances of the horizontal and vertical edges for fifteen distinct reconfigurable states are deduced from simulation results. Figures 11(a)–11(c) illustrate the real and imaginary impedances of all fifteen states. It is observed that for any frequency band, the impedance behavior of dual CP or LP states is similar to a great extent due to antenna symmetry which is clearly observed in Figure 11. The real part of the impedances is laid between the range of 100 and 250 Ω, as depicted in the figure. Correspondingly, the imaginary parts are nearly zero (~0 j). A judicious approach is made by considering the average edge impedance of around 160 Ω for all operating modes. Quarter wave matching sections are used to transform the impedance at 80 Ω at the coax end, as illustrated in Figure 10(a). The input impedance at the junction of the two feed lines is observed to vary within the range 50-100 Ω which would mismatch slightly with the 50 Ω coax feed but delivers enough matching to provide -10 dB reflection bandwidth for all the states. A slight offset in the impedance is noted after including the bias network in the design. Additional optimization of the feed network is done to achieve optimum impedance matching.

Table 2: Simulated and measured antenna parameter value.

Pol. state	Impedance BW(-10 dB)		Axial ratio BW (3 dB)		Realized gain (dBi)	
For 2.4 GHz band ($f2$)						
	S (MHz/%)	M (MHz/%)	S (MHz)	M (MHz)	S	M
HP	195/8	250/10			5.95	5.9
VP	190/8	350/14.3			5.75	5.65
45° slant	233/9.5	200/8.2			7.15	6.93
RHCP	542/22	758/31	110	150	5.73	5.49
LHCP	609/25	571/23.3	120	90	5.7	5.8
For 5.8 GHz band ($f1$)						
	S (MHz/%)	M (MHz/%)	S (MHz)	M (MHz)	S	M
HP	306/5.3	415/7.2			6.71	6.43
VP	433/7.5	630/11			7	6.89
45° slant	674/11.8	390/6.8			6.8	6.64
RHCP	683/12	645/11	170	130	6.75	6.51
LHCP	750/13	765/13.3	90	110	6.81	6.73
For 1.8 GHz band ($f3$)						
	S (MHz/%)	M (MHz/%)	S (MHz)	M (MHz)	S	M
HP	210/11.7	190/10.6			6.1	5.2
VP	170/9.4	210/11.7			6.05	5.8
45° slant	400/22	380/21			5.75	5.3
RHCP	420/23	430/24	90	120	5.96	5.44
LHCP	170/9.4	190/10.6	170	130	5.87	5.12

3.2. Biasing Network. Switching PIN diodes (model HPND-4005, Avago Technology) are incorporated in the design for the switching mechanism. In forward and reverse bias conditions, the diode shows low series and low resistances of 4.7 Ω and parallel capacitances of 0.017 pF, respectively. These switches exhibit low package parasitic along with improved isolation and insertion loss (0.4 dB). For proper diode biasing and coupling management, DC bias lines of width 0.2 mm and $0.3 \times 0.3\ mm^2$ bias pads are designed with proper layout on the antenna, as shown in Figure 10(a). 47 nH series inductors are placed on the bias line to block the RF component to the sources. Subsequently, series capacitances (33 pF) are incorporated in the bias network for RF signal continuity. The bias network and subsequent components are shown in the antenna diagram. The equivalent circuit models of the components are shown in Figure 10(b). The top and bottom views of the fabricated antenna are presented in Figures 10(c) and 10(d), respectively.

4. Measurement and Discussion

The radiation and impedance characteristics of the fabricated antenna are measured using a VNA with the model Agilent E5071B. A few precautionary measures are taken while conducting the measurement in an anechoic chamber. Spurious radiation from the open feed is prevented by covering it with absorbers, whereas the external DC wires are wrapped with aluminum paper to avoid coupling external radiation with the wires which may couple with the antenna radiation and cause pattern distortion. In spite, minute inconsistencies between the measured and simulated results are observed. These discrepancies are attributed to manual asymmetric soldering while fabricating the antenna and integrating the basic circuit model of the diodes in the simulation environment.

4.1. Reflection Coefficient (S_{11}). Impedance bandwidth for all fifteen operating modes is detailed in Table 2. Due to antenna symmetry, the input impedances (Z_{in}) and reflection coefficients for both the CP (RHCP and LHCP) and LP (VP and HP) states are observed to be comparable at any specific frequency band, as illustrated in Figure 12. In general, a single fundamental resonance for LP and dual orthogonal resonances for CP states are observed when the antenna is excited using individual orthogonal SMA feeds, as depicted in Figure 13(a). A similar trend is observed in all polarization states at three frequency bands while exciting the antenna using single SMA and coplanar edge-feed orthogonal microstrip lines. However, two additional higher harmonics in close proximity to the fundamental mode in HP and RHCP states at $f1$ and $f2$ bands are observed, as depicted in Figures 12(a) and 12(b), respectively. All other simulated and measured S_{11} are presented in Figures 12(c)–12(h).

This exception is observed in the real impedance plot at HP and RHCP states in $f1$ band, as illustrated in Figure 13(b). Interestingly, these higher order modes were not present when the antenna is excited by individual orthogonal feeds, as shown in Figure 13(a). Surface wave

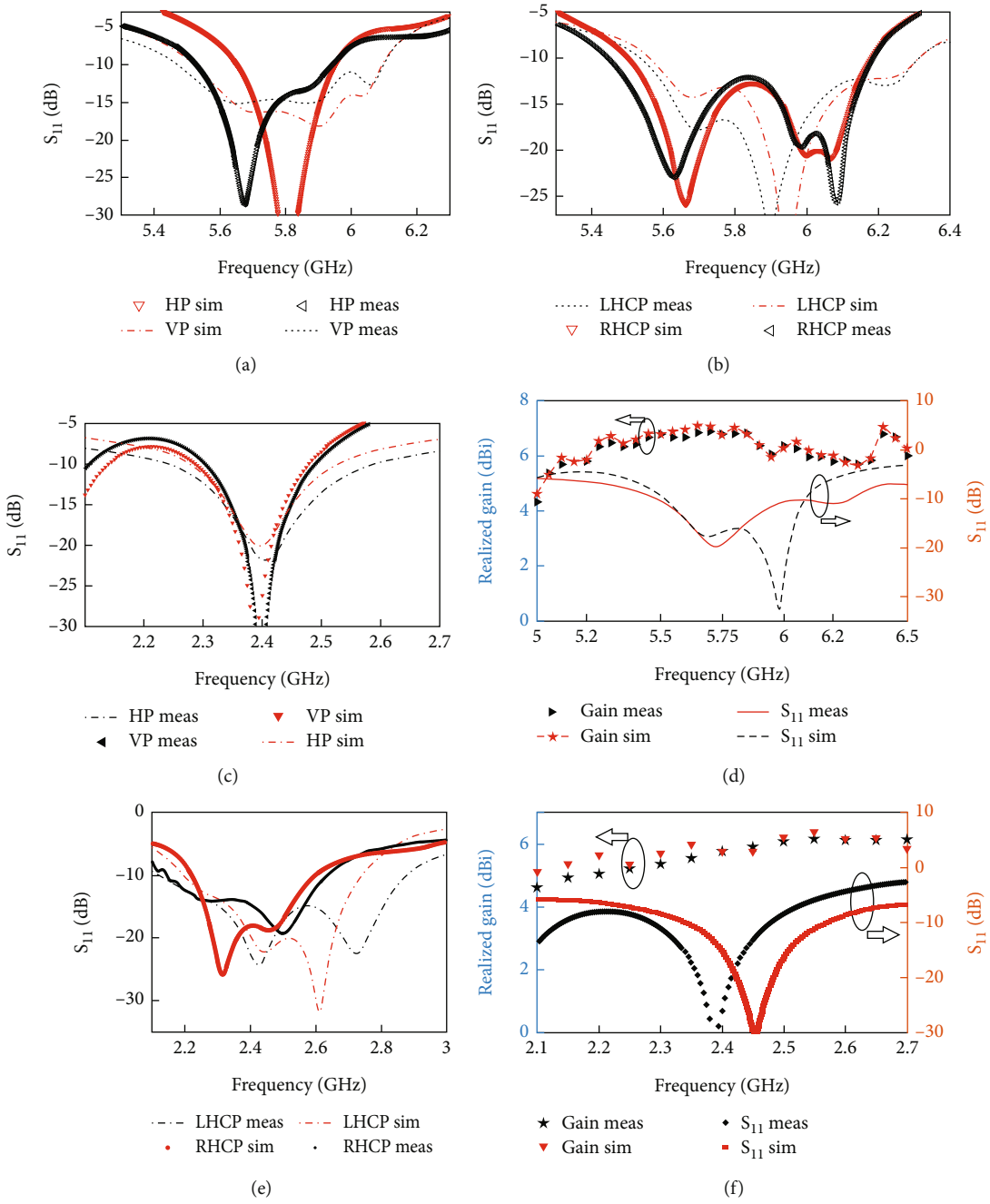

Figure 12: Continued.

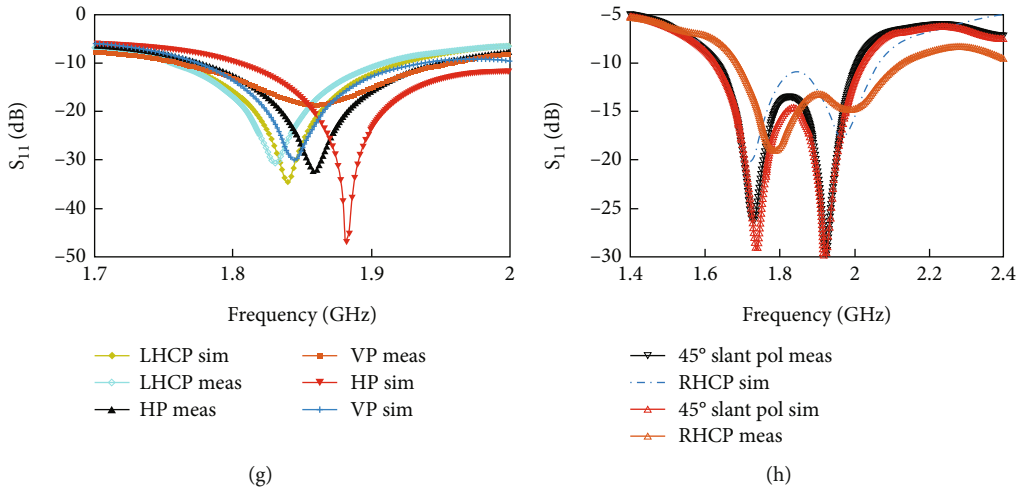

FIGURE 12: Simulated and measured reflection coefficients S_{11} for all polarization states (a) LP at $f1$, (b) CP at $f1$, (c) LP at $f2$, (d) 45° slant S_{11} and realized gain at $f1$, (e) CP at $f2$, (f) 45° slant S_{11}, and realized gain at $f2$, (g) LP and LHCP sates at $f3$ and, (h) RHCP and 45° slant states.

and radiation coupling from the orthogonal microstrip feed lines excites these modes, as depicted in Figure 13(b). Though the modal significance of the fundamental modes is found to be dominant, hence its characteristic is prominent over the band. As a result, the antenna performance remains unaltered except for the increment of impedance bandwidth in those specific states.

4.2. Radiation Pattern. Figure 14(a) illustrates the antenna radiation pattern for fifteen reconfigurable conditions at $\varphi = 0^\circ$ and $\varphi = 90^\circ$ planes. Due to antenna asymmetry, the pattern for LP or CP states operating in any given band is identical. Thus, HP and LHCP with 45° slant polarization states for each band are shown for brevity. Co and X-pol for a 45° slant are measured at $\varphi = 45\circ$ and $\varphi = 135\circ$ planes, respectively.

X-pol levels are measured below -15 dB for all modes in $\varphi = 0\circ$ and $\varphi = 90^\circ$ planes. HPBWs are measured to be nearly ±50° with slight variation for all the states in both planes, as depicted in the figures. Pattern invariance with negligible side lobe and X-pol level is also noted in a few states for comparatively wide impedance bandwidth modes, as shown in Figure 13, although minute offsets in measured patterns can be attributed to a variety of factors that have already been discussed. Figure 14(b) shows the 3D radiation pattern of all the fifteen reconfigurable states.

4.3. Realized Gain. Realized gains for all the reconfigurable states are depicted in Figures 12(d), 14(d), and 15(a)–15(f), respectively. The corresponding values are tabulated in Table 2. It is observed that broadside gains for all states are varied in the range of 5-7.2 dBi in both the principal planes. Simulated realized gains for either dual LPs or dual CPs for a specific band are largely similar due to antenna symmetry. The measured gains are slightly reduced primarily due to the fabrication tolerance, dielectric, conduction, diode, and lumped element losses.

4.4. Axial Ratio. Figures 16(a)–16(c) respect illustrate the simulated and measured AR bandwidth for the dual CP states at three frequency bands. Subsequently, the values are tabulated in Table 2 and observed good agreement.

Small discrepancies in the simulated and measured AR bandwidth are attributed to many influences as mentioned earlier.

4.5. Antenna Efficiencies. Antenna efficiency reduces with the internal resistance of the switching devices. The PIN switches that are used in the design are having large package parasitic capacitance and insertion loss. Diodes are biased accordingly to attain five different polarizations stated at three reconfigurable frequency bands, as shown in Table 1. Due to the presence of these lossy diodes at different biasing conditions, the efficiency of the antenna varies from 57% to 83%, as shown in Figure 17(a). Also, the usage of a lossy substrate introduces conduction and dielectric losses that further reduce the overall antenna efficiency. A forward biased diode draws a larger forward current, hence increases the diode ohmic loss and thus reduces the efficiency further. Two, four, and six numbers of diodes are turned ON subsequently to realize CP, LP, and 45° slant polarization states, as presented in Table 1. Thus, CP and 45° slant state show the highest and lowest efficiencies in the plot. Though antenna efficiencies can be improved significantly using low-loss switches, fabricating the designed antennas using a low tan δ (loss tangent) substrate also increases the total efficiency. Figure 17(b) depicts the total antenna efficiencies for five different polarization states at $f1$ band using low-loss switches and substrates. It shows clearly that $\eta(\%)$ has improved remarkably which varies from 88 to 97% for different polarization states at $f1$ band. In the other reconfigurable frequency bands ($f2$ and $f3$), similar improvement with slight variations in total efficiencies are observed and not shown for brevity.

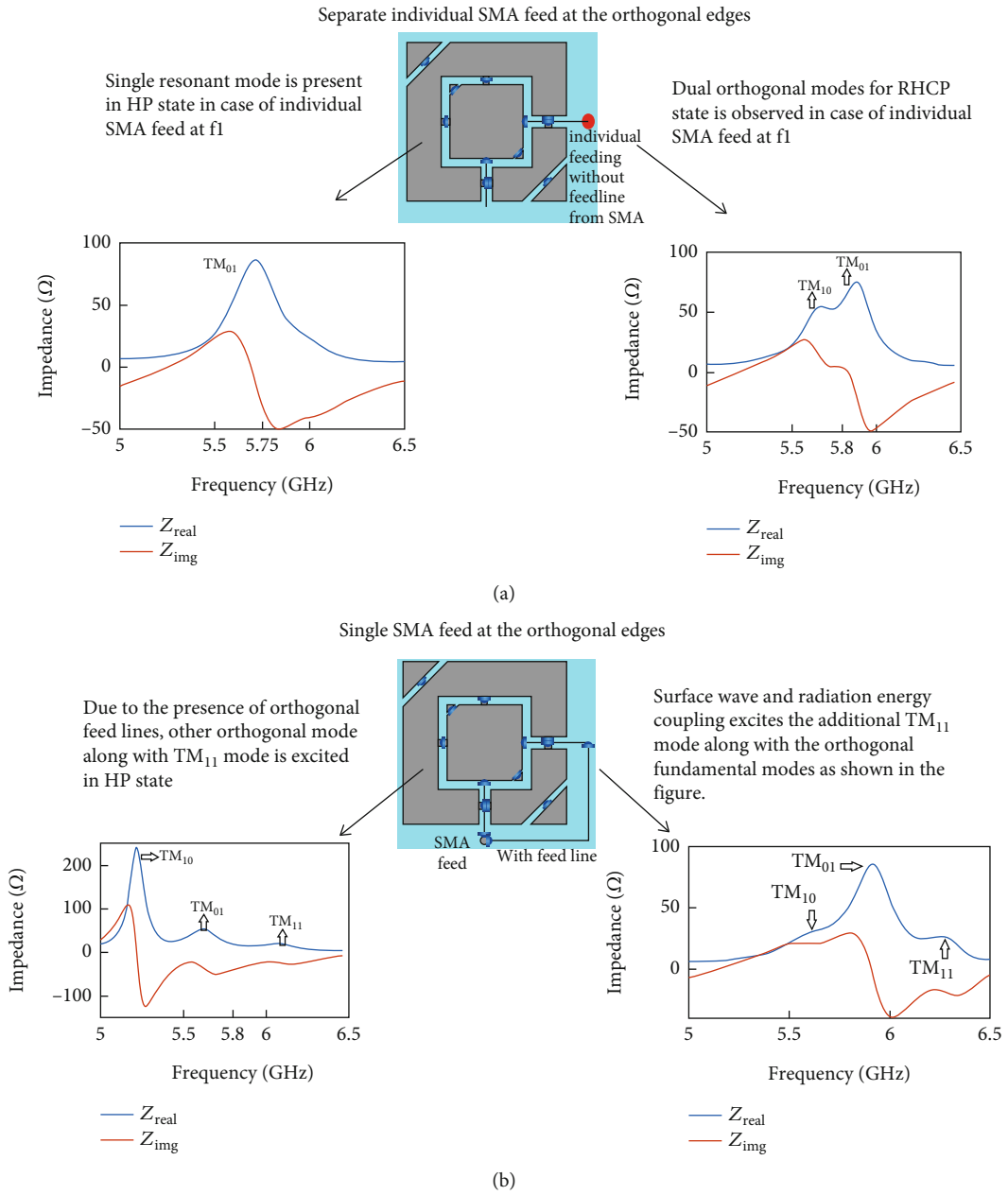

FIGURE 13: (a) Designed antenna with individual orthogonal SMA feed and corresponding resonances at $f1$ (5.8 GHz band). (b) Antenna with orthogonal microstrip line feed with corresponding resonances at $f1$ band.

4.6. Equivalent Circuit Model. The equivalent circuit model of any antenna only represents the terminal characteristics such as impedance or scattering characteristics. The radiation characteristics cannot be depicted using only the circuit model. Hence, authors have tried to present the operating model of three reconfigurable bands and subsequently the models for different operating polarizations in any specific band based on terminal characteristics.

Tri-band reconfigurability is realized by altering the antenna structure using switchable PIN diodes, as mentioned in the main manuscript. From a circuit point of view, a planar microstrip antenna can be represented using parallel RLC resonators. Thus, three such resonators with different R, L, and C values (representing different operating resonances) are connected in parallel using switching diodes to represent the three reconfigurable bands, as shown in Figure 18. Based on the biasing state of the diodes (ON or OFF), any specific operating band can be chosen to operate.

As discussed earlier, the frequency behavior of MSA can be modeled by parallel resonant circuit. Its constituent electrical parameters can further be computed from the knowledge of its resonant frequency (f_0) and quality factor (Q). In this study, the resistance at resonances is extracted from

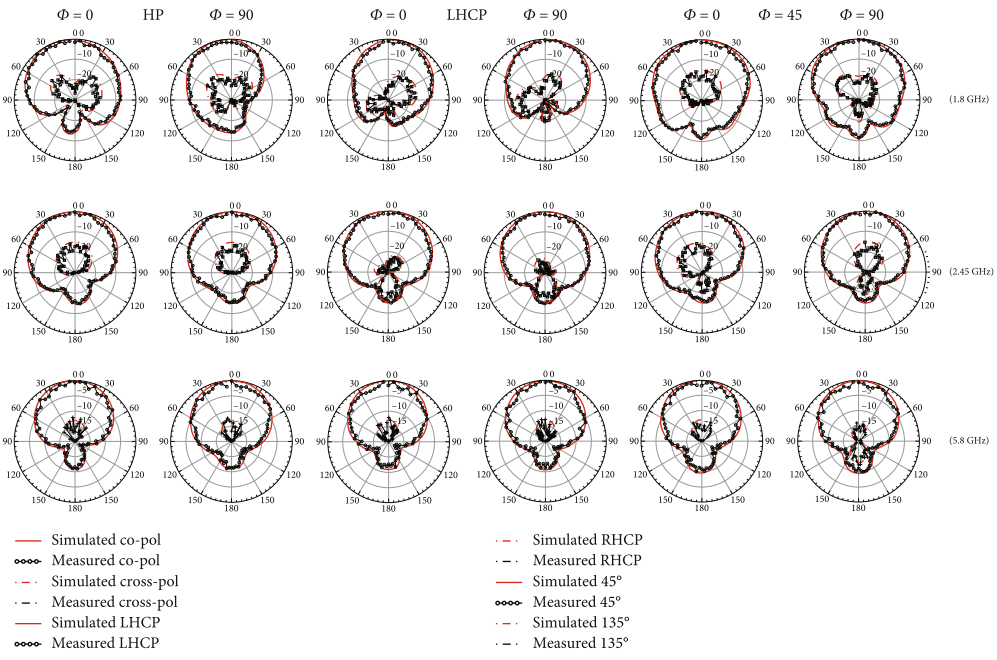

(a)

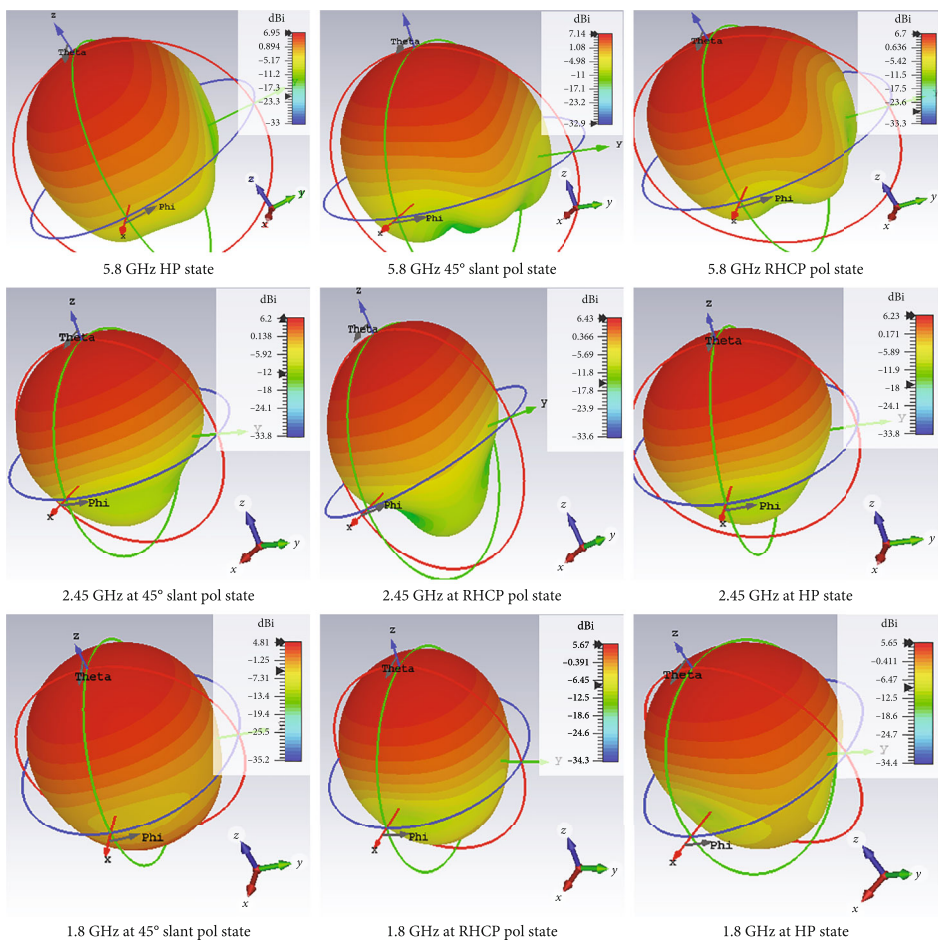

(b)

FIGURE 14: (a) Simulated and measured Co and X-pol pattern for (HP), (LHCP), and 45° slant $\varphi = 0^{\circ}$ and $\varphi = 90^{\circ}$ at 2.45 GHz, 5.8 GHz, and 1.8 GHz band. (b) Simulated 3D of all fifteen reconfigurable states at 2.45 GHz, 5.8 GHz, and 1.8 GHz band.

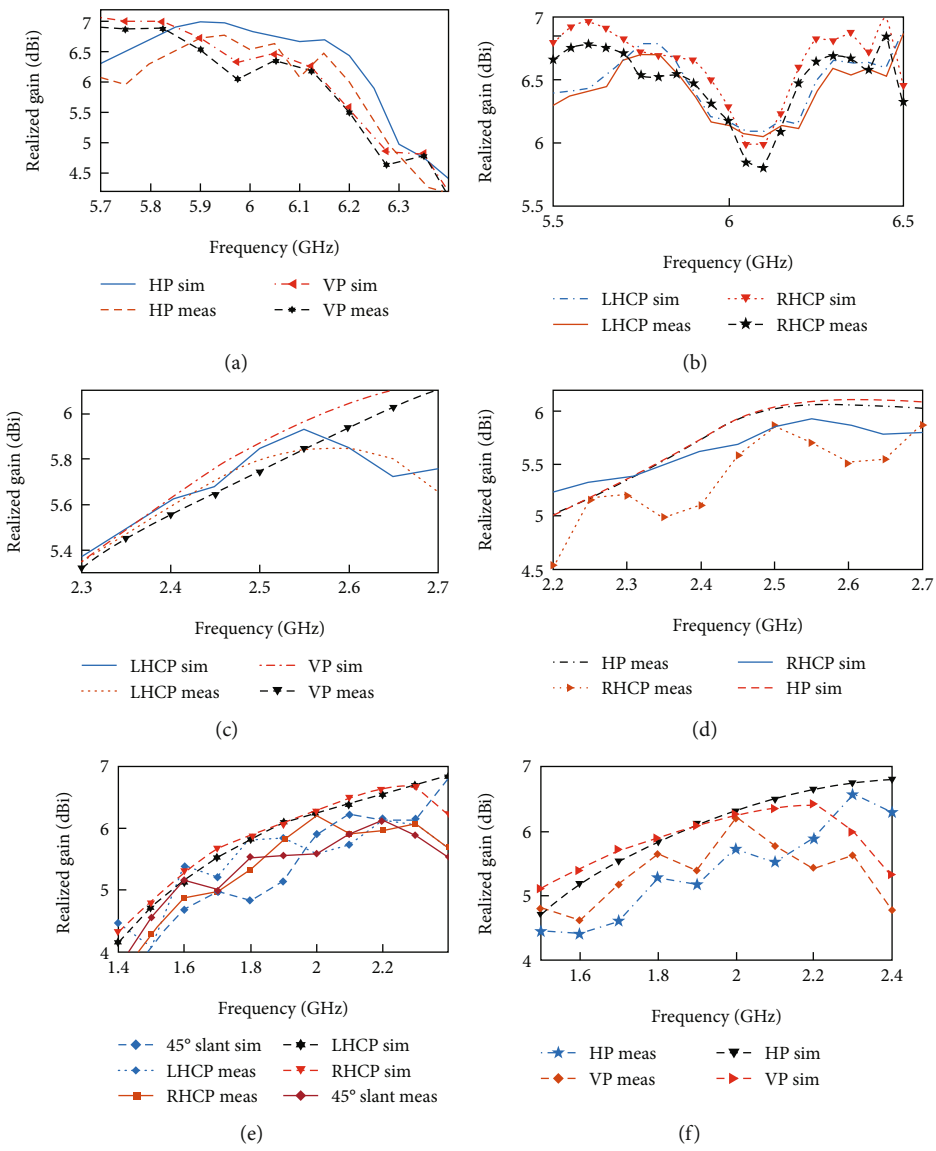

FIGURE 15: Realized gain for all reconfigurable states. (a) LP states at 5.8 GHz, (b) CP states at 5.8 GHz, (c) VP and LHCP states for 2.45 GHz, (d) HP and RHCP states for 2.45 GHZ, (e) dual CP and 45° slant for 1.8 GHz, and (f) LP for 1.8 GHz band. Meas: measured; Sim: simulated.

the full wave simulation, while the inductance (LMSA) and capacitance (CMSA) are calculated as follows:

$$L_{\mathrm{MSA}} = \frac{R}{\omega_0 Q} C_{\mathrm{MSA}} = \frac{1}{\omega_0^2 L_{\mathrm{MSA}}}. \tag{9}$$

Due to the antenna symmetry, the input impedances of dual CP or LP state at any operating band are comparable. Hence, the authors have derived the equivalent circuit model only for RHCP, HP, and 45° slant states at 5.8 GHz band. The results for the other states can be derived in the similar way and not shown here for brevity. Thus, only the equivalent circuit models for RHCP, HP, and 45° slant are shown in the figure. In general, a single fundamental resonance for LP and dual orthogonal resonances for CP states are observed when the antenna is excited using individual orthogonal SMA feeds, as depicted in Figure 13(a). Similar trend is observed in all polarization states at three frequency bands, which are illustrated in Figure 13. However, two additional higher harmonics in close proximity to the fundamental mode in HP and RHCP states at $f1$ band are observed as depicted in S_{11} plot in Figures 12(a) and 12(b). The below figures show the equivalent circuit models of RHCP (Figure 19(a)), HP (Figure 19(b)), and 45° (Figure 19(c)) states at 5.8 GHz band. It depicts the coexistence of three higher-order resonances coupled together. For the HP state, the resonance modes are inductively and capacitively coupled, as shown in Figure 3(b). Two distinct resonance modes are observed at 45° slant polarization within 5.7 to 6 GHz band, as shown in Figure 12(c). The models for other polarization states can be derived similarly.

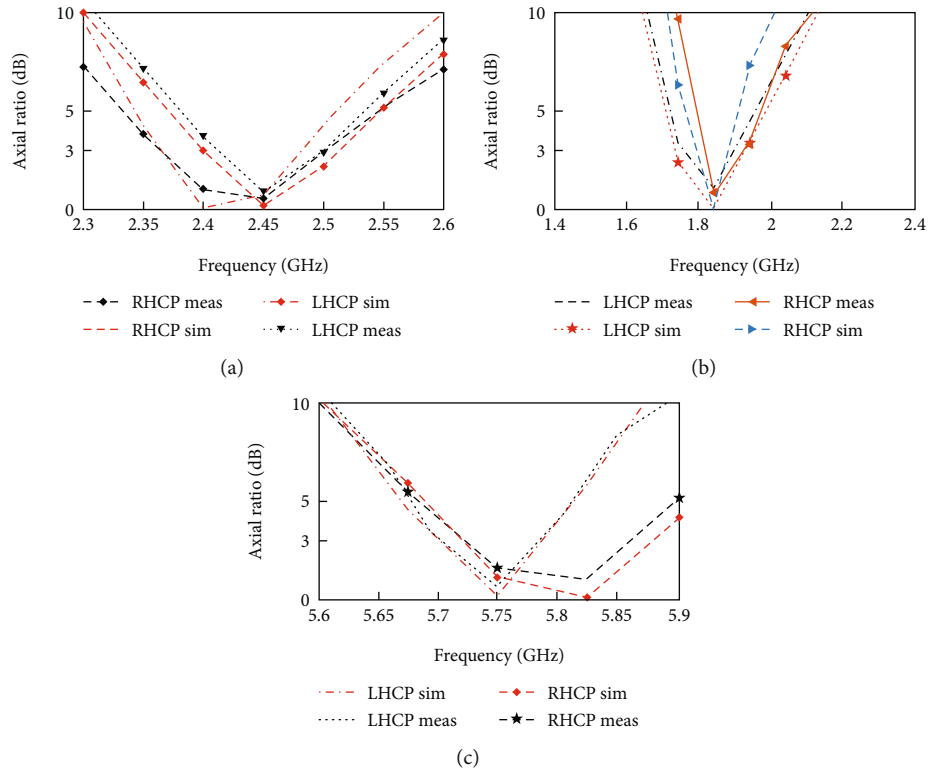

FIGURE 16: Simulated and measured 3 dB AR bandwidths of dual CP states at (a) 2.45 GHz, (b) 1.8 GHz, and (c) 5.8 GHz.

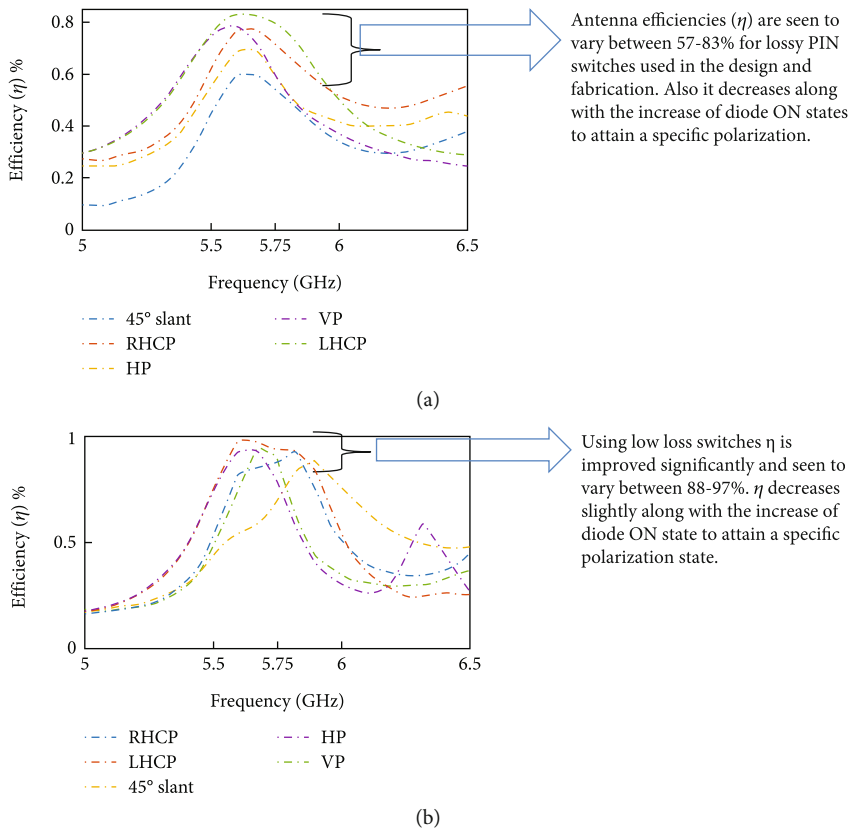

FIGURE 17: Total antenna efficiencies (η%) in $f1$ band operation using (a) lossy PIN diodes and (b) loss less PIN diodes in the antenna design.

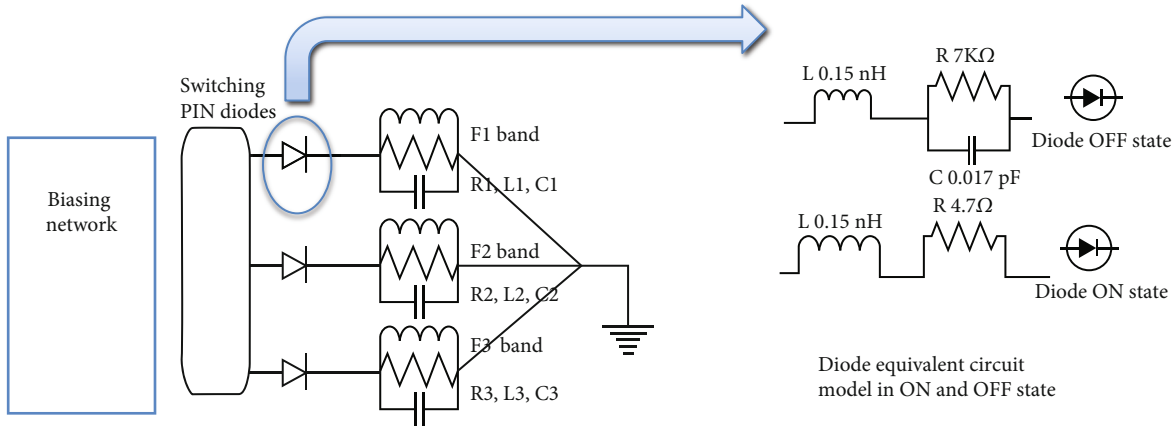

Figure 18: Equivalent circuit model of three reconfigurable bands based on the operation.

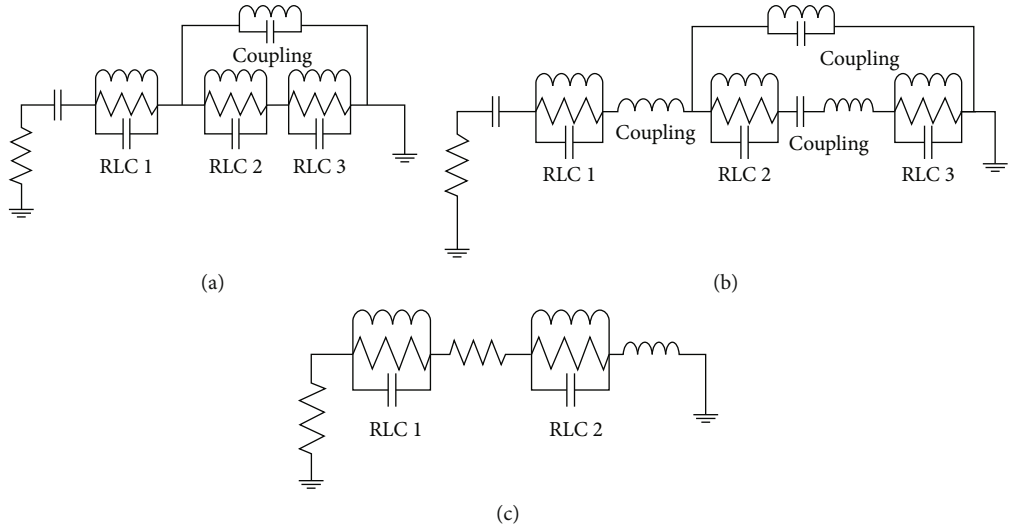

Figure 19: Equivalent circuit models for (a) RHCP state, (b) HP state, and (c) 45° slant polarization state.

Also, due to antenna symmetry, other CP and LP states depict similar models which are not shown for the sake of brevity.

S: simulated; M: measured.

5. Comparison and Discussion

In this section, the authors compare the proposed antenna with recently published work in the literature and subsequently discuss the advantages and novelty based on antenna flexibility, compactness, and overall performance in Table 3. Researchers in the open literature suggested maximum up-to-quad polarization states in three distinct frequency bands. It is worth noting that most authors in the open literature [8, 15–32] use multifeed, multilayered, and bulky structures, as well as complicated designs. To achieve frequency and pattern reconfigurability, the authors in the literature use a relatively broad footprint area in few cases [33, 34]. Also, a number of research articles published recently [35, 36] have shown continuous frequency tuning with multipolarization reconfigurability. A dual-polarized microstrip aperture array operates at three distinct frequency bands are illustrated in [37]. In [11], the authors employ exceedingly large numbers of PIN switches (48 nos) to attain four reconfigurable polarization states in three different operating bands. In [38], the authors demonstrate various reconfigurable polarization states over a broad frequency range. Penta-polarization reconfigurability utilizing a metasurface-inspired MSA slot antenna has only been proposed in one study so far [13]. In [39], authors have nicely explained the design methodology of a dual-CP (LHCP and RHCP) reconfigurable antenna in a wide frequency band using a truncated-corner patch and nonuniform metasurface as parasitic. The dual-layered single-feed antenna has depicted large operating bandwidth of 25.6% (-10 dB impedance and 3 dB Axial) with consistent realized gain and pattern. In [40], the authors have nicely presented a high gain Fabry-Perot resonator antenna with tri-polarization diversity (dual-CP and LP) in a tunable frequency band (7.3-7.6 GHz) using a partially reflective surface and a planar metallic reflector. The dual-layered high-profile (0.6λ) Fabry-Perot antenna with tri-polarization reconfigurability in 4% frequency tuning range has showed large gain (15.1 dBi) and it is suitable for

Table 3: Antenna parameter comparison between proposed and recently published works.

Ref.	No. of flexibilities	Resonant (GHz)	Frequency agility	Substrate layers (nos.)	Polarization agility	Peak gain	% impedance BW	Footprint area (λ_0^2)	No. of diodes	Antenna height(λ_0)
[38]	8	5.2/5.8	2	1	4	3	3.5/3.6	1×1.1	6 PIN	0.08
[34]	3	8-11.2	1	2	3	16.5	33 tuning	2.5×2.5	NA	0.725
[17]	6	5.2/5.7	2	1	3	5.81	4-8	1.1×1	7 PIN	0.04
[36]	4	5.7	1	3	4	9.9-10.3	23/27 (LP & CP)	2.64×2.83	4 SDPT	0.062
[33]	4	3.5/5.2	2	2	2	6.86/8.14	21.7/25	0.78×0.87	4 PIN	0.1
[12]	10	5.2/5.8	2	1	5	5-7.5	7-31 (LP and CP)	0.5×0.5	10 PIN	<0.01
[11]	12	2.25-2.45	3	1	4	4.7	33.9	0.86×0.78	48 PIN	0.01
[16]	3	3.6-4	1	1	3	5-10	10 tuning	1.4×1.4	2 varactor	0.01
[20]	3	2.4-3.6	1	1	3	2.6-7.3	40 tuning (CP and LP)	1.2×1.1	12 varactor	0.04
[35]	8	2.2-3	4	3	2	-1 to 9	NA	2×0.67	32 PIN, 24 Varactor	0.18
[13]	5	5.2	1	2	5	8.2	28	1.21×1.21	15 PIN	0.06
[39]	2	4.76-6.16	1	2	2	7.3	25.6	0.88×0.88	02	0.05
[40]	3	7.3-7.6	1	2	3	15.1	(4% tuning)	2×2	02	0.6
This work	15	5.8/2.4/1.8	3	1	5	5.1-7	6.8-31 (LP and CP)	0.96×0.96	15 PIN	<0.01

satellite application as claimed by the expert authors. We also propose a simple, compact frequency and polarization agile MSA with ten reconfigurable states in our previous paper [12]. Recent proposals in the literature have visible flaws, such as complicated feed networks, multilayer assembly, and multiple SMA feeds, which would make real-world implementation difficult. The proposed antenna, on the other hand, has a number of distinct advantages, including a substantially smaller structure. From an RF aspect, the proposed design can be implemented into the transreceivers system design to alleviate SINR, BER, or fluctuating RSS concerns, among other issues. As a result, the antenna is well suited for sophisticated multifunctional applications as well as preventing interference and multipath difficulties in electromagnetically dense situations.

6. Conclusion

The wireless front is gradually getting denser due to the deployment of a large number of nodes in close proximity to enhance data bandwidth and network coverage to cater to a wide range of advanced and real-time applications. Due to the constraint in the usable RF spectrum, there is a significant overlapping of operating frequency bans, resulting in low SINR and high BER. In this article, the authors put forward a method to mitigate these issues from an RF viewpoint by designing a multifunctional antenna. This approach would certainly provide greater flexibilities to the system designers, with fifteen available reconfigurable states of the prototype antenna to counter these concerns. In this study, a compact, reconfigurable MSA is introduced in the literature for the very first time, with five polarizations reconfigurable at each of three reconfigurable frequency bands. A prototype MSA with three distinct reconfigurable bands operating at 1.8 GHz, 2.4 GHz, and 5.8 GHz is designed and fabricated. The simulated antenna is measured for fifteen reconfigurable states and observed acceptable results. The design can also be scaled to other operating bands, hence applicable for a wide range of applications. The antenna can readily be combined with conventional transreceiver systems due to its single-feed and compact structure. Therefore, the design simplicity, compactness, fabrication ease, and optimum performance make the proposed design very suitable in the ultradense environment.

Data Availability

Data is with the manuscript.

Conflicts of Interest

The authors declare that they have no conflicts of interest.

Acknowledgments

This study was supported by the Council of Scientific and Industrial Research (CSIR) (Acknowledgment No: 1431235/2K19/1, Award File No: 09/096(1038)/2021-EMR-I, and dated 12.03.2021).

References

[1] C. Guo, F. Liu, S. Chen, C. Feng, and Z. Zeng, "Advances on exploiting polarization in wireless communications: channels, technologies, and applications," *IEEE Communications Surveys & Tutorials*, vol. 19, no. 1, pp. 125–166, 2017.

[2] R. Borralho, A. Mohamed, A. U. Quddus, P. Vieira, and R. Tafazolli, "A survey on coverage enhancement in cellular networks: challenges and solutions for future deployments," *IEEE Communications Surveys & Tutorials*, vol. 23, no. 2, pp. 1302–1341, 2021.

[3] S. Ahmed and M. Faulkner, "Interference issues at co-located base stations and an adaptive cancellation solution," in *2010 Electromagnetic Compatibility Symposium - Melbourne*, pp. 1–4, Melbourne, VIC, Australia, 2010.

[4] M. G. Amin, "Interference mitigation in spread spectrum communication systems using time-frequency distributions," *IEEE Transactions on Signal Processing*, vol. 45, no. 1, pp. 90–101, 1997.

[5] N. Mishra, D. Mishra, N. Gajjar, and K. Parmar, "Advanced digital signal processing for interference mitigation in very high throughput satellite," in *Advances in Intelligent Systems and Computing*, F. Thakkar, G. Saha, C. Shahnaz, and Y. C. Hu, Eds., Springer, Singapore, 2022.

[6] P. Jacob, A. S. Madhukumar, and A. Alphones, "Interference mitigation through cross polarized transmission in femto-macro network," *IEEE Communications Letters*, vol. 17, no. 10, pp. 1940–1943, 2013.

[7] D. Chen, W. Yang, W. Che, Q. Xue, and L. Gu, "Polarization-reconfigurable and frequency-tunable dipole antenna using active AMC structures," *IEEE Access*, vol. 7, pp. 77792–77803, 2019.

[8] Z. Li, J. Han, Y. Mu, X. Gao, and L. Li, "Dual-band dual-polarized base station antenna with a notch band for 2/3/4/5G communication systems," *IEEE Antennas and Wireless Propagation Letters*, vol. 19, no. 12, pp. 2462–2466, 2020.

[9] M. Golmohamadi, A. Narbudowicz, and J. Frolik, "Mitigating indoor channels with quad-polarization diversity," *IEEE Antennas and Wireless Propagation Letters*, vol. 18, no. 6, pp. 1199–1202, 2019.

[10] D. K. Singh, B. K. Kanaujia, S. Dwari, and G. P. Pandey, "Multi band multi polarized reconfigurable circularly polarized monopole antenna with simple biasing network," *AEU - International Journal of Electronics and Communications*, vol. 95, pp. 177–188, 2018.

[11] L. Ge, Y. Li, J. Wang, and C. Sim, "A low-profile reconfigurable cavity-backed slot antenna with frequency, polarization, and radiation pattern agility," *IEEE Transactions on Antennas and Propagation*, vol. 65, no. 5, pp. 2182–2189, 2017.

[12] J. Pal, K. Patra, and B. Gupta, "A low profile single feed compact dual-band penta-polarization agile microstrip antenna for interference mitigation in point to point link in ultra-dense environment," *AEU-International Journal of Electronics and Communications*, vol. 150, 2022.

[13] P. Liu, W. Jiang, S. Sun, Y. Xi, and S. Gong, "Broadband and low-profile penta-polarization reconfigurable metamaterial antenna," *IEEE Access*, vol. 8, pp. 21823–21831, 2020.

[14] G. Ramesh, B. Prakash, B. Inder, and I. Apisak, *Circularly Polarized Microstrip Antenna and Techniques in Microstrip Antenna Design Handbook*, Artech House, Norwood, MA, USA, 2001.

[15] F. A. Ghaffar, M. Vaseem, L. Roy, and A. Shamim, "Design and fabrication of a frequency and polarization reconfigurable microwave antenna on a printed partially magnetized ferrite substrate," *IEEE Transactions on Antennas and Propagation*, vol. 66, no. 9, pp. 4866–4871, 2018.

[16] M. Ikram, N. Nguyen-Trong, and A. Abbosh, "A simple single-layered continuous frequency and polarization-reconfigurable patch antenna array," *IEEE Transactions on Antennas and Propagation*, vol. 68, no. 6, pp. 4991–4996, 2020.

[17] R. K. Singh, A. Basu, and S. K. Koul, "A novel reconfigurable microstrip patch antenna with polarization agility in two switchable frequency bands," *IEEE Transactions on Antennas and Propagation*, vol. 66, no. 10, pp. 5608–5613, 2018.

[18] B. Anantha, L. Merugu, and P. V. D. S. Rao, "A novel single feed frequency and polarization reconfigurable microstrip patch antenna," *AEU - International Journal of Electronics and Communications*, vol. 72, pp. 8–16, 2017.

[19] J. Hu and Z.-C. Hao, "Design of a frequency and polarization reconfigurable patch antenna with a stable gain," *IEEE Access*, vol. 6, pp. 68169–68175, 2018.

[20] N. Nguyen-Trong, L. Hall, and C. Fumeaux, "A frequency- and polarization-reconfigurable stub-loaded microstrip patch antenna," *IEEE Transactions on Antennas and Propagation*, vol. 63, no. 11, pp. 5235–5240, 2015.

[21] W. Li, Y. M. Wang, Y. Hei, B. Li, and X. Shi, "A compact low-profile reconfigurable metasurface antenna with polarization and pattern diversities," *IEEE Antennas and Wireless Propagation Letters*, vol. 20, no. 7, pp. 1170–1174, 2021.

[22] C. Zhou, B. Wang, and H. Wong, "A compact dual-mode circularly polarized antenna with frequency reconfiguration," *IEEE Antennas and Wireless Propagation Letters*, vol. 20, no. 6, pp. 1098–1102, 2021.

[23] J. Pal, K. Patra, and B. Gupta, "A TM_{03} mode reduced side lobe high-gain printed antenna array in K band for UDN and IoTapplications in 5G," *International Journal of RF and Microwave Computer-Aided Engineering*, vol. 30, 2020.

[24] A. Arbelaez, I. Goode, J. Gomez-Cruz, C. Escobedo, and C. E. Saavedra, "Liquid metal reconfigurable patch antenna for linear, RH, and LH circular polarization with frequency tuning," *Canadian Journal of Electrical and Computer Engineering*, vol. 43, no. 4, pp. 218–223, 2020.

[25] Y. Liu, Q. Wang, Y. Jia, and P. Zhu, "A frequency- and polarization-reconfigurable slot antenna using liquid metal," *IEEE Transactions on Antennas and Propagation*, vol. 68, no. 11, pp. 7630–7635, 2020.

[26] A. Bharathi, M. Lakshminarayana, and P. V. D. S. Rao, "A quad-polarization and frequency reconfigurable square ring slot loaded microstrip patch antenna for WLAN applications," *AEU - International Journal of Electronics and Communications*, vol. 78, pp. 15–23, 2017.

[27] J.-Y. Liu, R. X. Li, and S.-G. Zhou, "A reconfigurable printed antenna with frequency and polarization diversity based on bow-tie dipole structure," *IEEE Transactions on Antennas and Propagation*, vol. 67, no. 12, pp. 7628–7632, 2019.

[28] L. S. Yang, L. Yang, Y. A. Zhu, K. Yoshitomi, and H. Kanaya, "Polarization reconfigurable slot antenna for 5.8 GHz wireless applications," *AEU - International Journal of Electronics and Communications*, vol. 101, pp. 27–32, 2019.

[29] M. Mani, R. Moolat, S. V. Abdulrahiman, A. P. Viswanathan, V. Kesavath, and M. Pezholil, "Frequency reconfigurable stepped impedance dipole antenna for wireless applications," *AEU - International Journal of Electronics and Communications*, vol. 115, article 153029, 2020.

[30] T. Prakash, R. K. Chaudhary, and R. K. Gangwar, "A reconfigurable active microstrip antenna for agile switching: pattern, beamwidth, and multibeam," *AEU - International Journal of Electronics and Communications*, vol. 149, article 154181, 2022.

[31] A. Bhattacharyya, J. Pal, K. Patra, and B. Gupta, "Bandwidth-enhanced miniaturized patch antenna operating at higher order dual-mode resonance using modal analysis," *IEEE Antennas and Wireless Propagation Letters*, vol. 20, no. 2, pp. 274–278, 2021.

[32] S. Ullah, S. Hayat, A. Umar, U. Ali, F. A. Tahir, and J. A. Flint, "Design, fabrication and measurement of triple band frequency reconfigurable antennas for portable wireless communications," *AEU - International Journal of Electronics and Communications*, vol. 81, pp. 236–242, 2017.

[33] Z. Nie, H. Zhai, L. Liu, J. Li, D. Hu, and J. Shi, "A dual-polarized frequency-reconfigurable low-profile antenna with harmonic suppression for 5G application," *IEEE Antennas and Wireless Propagation Letters*, vol. 18, no. 6, pp. 1228–1232, 2019.

[34] C. Ni, M. S. Chen, Z. X. Zhang, and X. L. Wu, "Design of frequency-and polarization-reconfigurable antenna based on the polarization conversion metasurface," *IEEE Antennas and Wireless Propagation Letters*, vol. 17, no. 1, pp. 78–81, 2018.

[35] J. Hu, X. Yang, L. Ge, Z. Guo, Z. C. Hao, and H. Wong, "A reconfigurable 1×4 circularly polarized patch array antenna with frequency, radiation pattern, and polarization agility," *IEEE Transactions on Antennas and Propagation*, vol. 69, no. 8, pp. 5124–5129, 2021.

[36] J. Hu, Z. C. Hao, and W. Hong, "Design of a wideband quad-polarization reconfigurable patch antenna array using a stacked structure," *IEEE Transactions on Antennas and Propagation*, vol. 65, no. 6, pp. 3014–3023, 2017.

[37] S. S. Zhong, Z. Sun, L.-B. Kong, C. Gao, W. Wang, and M.-P. Jin, "Tri-band dual-polarization shared-aperture microstrip array for SAR applications," *IEEE Transactions on Antennas and Propagation*, vol. 60, no. 9, pp. 4157–4165, 2012.

[38] Y. P. Selvam, L. Elumalai, M. G. N. Alsath, M. Kanagasabai, S. Subbaraj, and S. Kingsly, "Novel frequency- and pattern-reconfigurable rhombic patch antenna with switchable polarization," *IEEE Antennas and Wireless Propagation Letters*, vol. 16, pp. 1639–1642, 2017.

[39] H. H. Tran, C. D. Bui, N. Nguyen-Trong, and T. K. Nguyen, "A wideband non-uniform metasurface-based circularly polarized reconfigurable antenna," *IEEE Access*, vol. 9, pp. 42325–42332, 2021.

[40] H. H. Tran and H. C. Park, "A simple design of polarization reconfigurable Fabry-Perot resonator antenna," *IEEE Access*, vol. 8, pp. 91837–91842, 2020.